ACCSCIENCE PUBLISHING

International Journal of Bioprinting

RESEARCH ARTICLE

Construction of gelatin–alginate scaffolds containing chondrocytes using 3D bioprinting technology for the study of *in vitro* cartilage senescence

Hanxiao Qin[1†], Fanqing Xu[1†], Jianfeng Li[2*], and Yi Ding[1*]

[1]Department of Spine Surgery, Ganzhou People's Hospital, Ganzhou, Jiangxi, China

[2]Innovation Platform of Regeneration and Repair of Spinal Cord and Nerve Injury, Department of Orthopedics Surgery, The Seventh Affiliated Hospital, Sun Yat-sen University, Shenzhen, Guangdong, China

Abstract

Osteoarthritis (OA) is an age-related degenerative joint disease characterized by progressive cartilage deterioration. Chondrocyte senescence is recognized as a key contributor to the onset and progression of OA. Establishing reliable cartilage senescence models is, therefore, essential for elucidating the underlying mechanisms and developing preventive strategies for OA. 3D-bioprinted models offer significant advantages in precisely controlling tissue architecture, enabling spatial delivery of bioactive molecules, and supporting dynamic cell culture. In this study, we employed 3D bioprinting technology to construct cartilage models and subsequently established cartilage senescence models using hydrogen peroxide (H_2O_2). Firstly, gelatin–sodium alginate hydrogel scaffolds provided favorable mechanical strength and porosity, creating a supportive microenvironment for chondrocyte proliferation. Secondly, these scaffolds exhibited excellent biocompatibility and effectively promoted extracellular matrix synthesis and secretion. By comparing H_2O_2-induced 2D chondrocyte senescence models with 3D-bioprinted cartilage senescence models, our results demonstrated that the 3D models more closely mimicked the molecular characteristics of naturally aged human cartilage. Therefore, the 3D-bioprinted cartilage senescence models represent a promising experimental platform for investigating the pathogenesis and prevention of age-related OA.

Keywords: 2D chondrocyte senescence; 3D bioprinting; 3D cartilage senescence; Articular cartilage-laden scaffolds; Bioactive bioink

1. Introduction

Articular cartilage is a specialized connective tissue that lacks vascular, neural, and lymphatic systems. It possesses unique biomechanical properties, including toughness and viscoelasticity, which are essential for its roles in load-bearing and providing lubrication during joint movement.[1,2] However, defects in articular cartilage—caused by traumatic injury, chronic inflammation, or aging—can lead to serious clinical manifestations, such as joint pain, impaired mobility, and irreversible joint dysfunction.[3]

†These authors contributed equally to this work.

***Corresponding authors:**
Yi Ding
(dingyi@mail.gzsrmyy.com)

Jianfeng Li
(lijf68@mail3.sysu.edu.cn)

Citation: Qin H, Xu F, Li J, Ding Y. Construction of gelatin–alginate scaffolds containing chondrocytes using 3D bioprinting technology for the study of *in vitro* cartilage senescence. *Int J Bioprint*. 2025;11(4):189-208. doi: 10.36922/IJB025150136

Received: April 11, 2025
1st revised: May 12, 2025
2nd revised: May 22, 2025
Accepted: May 27, 2025
Published online: May 30, 2025

If left untreated, these lesions often progress to degenerative conditions such as osteoarthritis (OA). The World Health Organization (WHO) estimates that the global population affected by OA will approach 1 billion by 2030, placing a significant burden on healthcare systems and household economies worldwide.[4] Cellular senescence within OA-affected joints has been identified as a key contributor to disease pathogenesis.[5,6] Increasing evidence demonstrates that senescence-associated changes occur in several joint components, including cartilage, synovium, and meniscus.[7,8] Nevertheless, there remains a lack of suitable models to investigate the relationship between cartilage and OA progression. Developing cartilage aging models is, therefore, essential for studying the pathogenesis and advancement of OA.

In recent decades, research has focused on elucidating the mechanisms of chondrocyte senescence, identifying therapeutic agents, and optimizing treatment strategies using various experimental models-including animal models, 2D cell cultures, and advanced 3D systems.[9,10] Current animal models used to study chondrocyte senescence typically rely on natural aging or surgical interventions in combination with gene knockouts targeting anti-senescence pathways.[11] For example, histological analysis of 18-month-old guinea pigs has revealed moderate to severe chondrocyte senescence, characterized by significant reductions in proteoglycan and collagen content, closely mimicking human cartilage degeneration.[12] Additionally, in *Del1* heterozygous (*Del1*+/−) mice, histological assessments from 3 to 22 months of age displayed accelerated knee cartilage degeneration due to impaired type II collagen gene expression.[13] However, despite their relevance, animal models present several limitations, including long experimental durations and high costs, which restrict their use in large-scale OA research.[14]

In contrast, 2D models offer simplicity, convenience, and high experimental control, and have been widely adopted across various research areas.[15] For instance, hydrogen peroxide (H_2O_2) treatment has been reported to induce oxidative and inflammatory stress in rat chondrocytes, promoting cellular senescence.[16] Nevertheless, 2D systems fall short in recapitulating the biomechanical cues, as well as the complex cell–cell and cell–matrix interactions present in native cartilage tissue.[17] To address these limitations, 3D culture technologies have been developed to more accurately mimic *in vivo* conditions. These models retain the advantages of 2D systems while offering a microenvironment that better preserves cellular phenotype and behavior. 3D culture models can be broadly categorized into scaffold-free 3D cell cultures, scaffold-based systems, explant models, bioreactors, organoids, organ-on-a-chip platforms, and 3D-bioprinted constructs.[18]

Scaffold-free 3D culture systems simulate *in vivo* cell growth conditions without external matrices or supports.[19] Co-culturing articular chondrocytes (ACs) with mesenchymal stem cells and chitosan/hyaluronic acid nanoparticles has been reported to promote chondrogenic differentiation.[20] However, these models are limited by high cultivation costs, short cell viability, and increased susceptibility to apoptosis. Scaffold-based 3D models, developed to overcome the limitations of scaffold-free systems provide a more physiologically relevant tissue-like environment. These models support more native-like 3D cellular behaviors. Embedding chondrogenic factors into hydrogel matrices for cell encapsulation has been demonstrated to enhance cartilage formation.[21] Although several issues remain, such as high cost, limited scalability, slow proliferation, and challenges in standardization, continued refinement is needed to improve model reliability.

Explant models involve the *in vitro* culture of tissue samples excised from live organisms under sterile conditions.[22] For example, treating cartilage explants with interleukin-1β can induce chondrocyte senescence.[23] However, limitations include technical complexity, inability to fully mimic the *in vivo* microenvironment, and species-specific differences, all of which must be addressed through technological and methodological advances. Bioreactors provide dynamic culture conditions under tightly controlled parameters and have been used to separate cartilage and bone units independently. While promising, their application is hindered by high maintenance costs, operational complexity, and membrane contamination risks.[24]

Organoids, which are 3D structures derived from adult or pluripotent stem cells, have gained attention for their ability to mimic real organ architecture and function. They offer advantages over traditional 2D cultures and patient-derived explants in terms of structural fidelity and genetic similarity.[25] For instance, human periosteum-derived cells have been demonstrated to self-assemble *in vitro* and form bone organoids capable of autonomous regeneration upon transplantation into mice.[26] Despite rapid progress, organoids still only partially reproduce native organ functions and are often limited in longevity and physiological complexity.[27,28]

Organ-on-a-chip systems combine microfluidics and 3D printing technologies to replicate the microarchitecture of organs on a chip.[29] A human-induced pluripotent stem cells-derived osteochondral chip has been used to simulate

OA-related pathology and effectively model bone–cartilage interactions under both healthy and diseased conditions.[30] However, this technology faces challenges in terms of reproducibility, organ maturity, and the integration of key elements, such as vasculature, innervation, and immune cells. Further technical development is essential for expanding its utility in disease modeling and drug screening.[31,32]

3D bioprinting represents a cutting-edge platform that enables the fabrication of living tissues using bioinks composed of cells, growth factors, and biocompatible materials.[33] Compared to other 3D models, bioprinting offers superior spatial precision, structural fidelity, and mechanical tunability, making it especially attractive for regenerative medicine and disease modeling. In cartilage tissue engineering, the scaffold material must possess excellent biocompatibility, mechanical integrity, and support for cellular activity.[34,35] Gelatin (Gel) and sodium alginate (Alg) are widely used in 3D bioprinting due to their favorable biological properties and printability. Recent studies have successfully encapsulated chondrocytes in Gel–Alg hydrogels using bioprinting, maintaining high cell viability and regional gene expression.[36–39] Another study developed Gel–Alg-based bioinks crosslinked with calcium chloride to fabricate scaffolds with robust mechanical properties and biocompatibility. These scaffolds supported long-term chondrocyte survival and functionality *in vitro* and demonstrated effective cartilage repair *in vivo*.[39]

In this study, we established a novel cartilage senescence model using Gel–Alg hydrogels at three different concentration ratios. ACs were encapsulated in 3D-bioprinted constructs, followed by H_2O_2-induced senescence. The innovation lies in the integration of biofabricated cartilage with precisely engineered structural and biochemical cues, coupled with oxidative stress-induced aging. This two-stage modeling strategy, which mimics age-related cartilage degeneration, has not been reported in current OA models (Figure 1). The resulting platform provides a physiologically relevant microenvironment that supports AC viability, maintains region-specific phenotypic markers, and reproduces senescence-associated changes under oxidative stress. This 3D-bioprinted cartilage senescent model offers a promising experimental system for investigating OA pathogenesis and developing targeted therapeutic interventions.

2. Materials and methods

2.1. Preparation of bioinks

Three different Gel–Alg bioink formulations were prepared for the 3D bioprinting of hydrogel scaffolds: 7% Gel + 3% Alg (7 Gel–3 Alg), 8% Gel + 2% Alg (8 Gel–2 Alg), and 9% Gel + 1% Alg (9 Gel–1 Alg). Briefly, accurately weighed amounts of 7% Gel (3.5 g) and 3% Alg (1.5 g) (Biosharp, China) were UV-sterilized (254 nm) for 3 h. The sterilized powders were then aseptically transferred into a 50 mL centrifuge tube containing 10 mL of culture medium. The tube was sealed with parafilm to maintain sterility. The mixture was homogenized by continuous agitation at 150 rpm in a 60°C incubator shaker for 3 h to ensure complete dissolution.[40] The resulting bioinks were loaded into 3D bioprinting cartridges using sterile 3 mL Pasteur pipettes and centrifuged at 800 rpm for 3 min to remove air bubbles. The prepared bio-inks were stored at 4°C and remained stable for up to 7 days.

2.2. Viscosity and printability of bioinks

To assess the viscoelastic properties of Gel–Alg bioinks with three different concentration ratios, a rotational rheometer (Thermo Fisher, United States of America [USA]) was employed. Briefly, the bioinks were thoroughly mixed to eliminate air bubbles and then loaded between the parallel plates of the rheometer, with the initial gap set at 1 mm. Shear rates ranging from 0.1 to 1000 s^{-1} were applied, and measurements were conducted at a constant temperature of 25°C. The viscosity (η) versus shear rate curve was recorded to evaluate the shear-thinning behavior of the bioinks.

2.3. Fabrication of 3D-bioprinted scaffolds

Hydrogel scaffolds were fabricated using 3D bioprinting technology. Briefly, a stereolithography file of the scaffold model was designed using Autodesk Fusion 360 CAD software (Figure 2A) and imported into a 3D bioprinter (Regenovo, China) for fabrication. Gel and Alg were selected as the scaffold materials. A nozzle with an inner diameter of 0.34 mm was used, and scaffolds were printed layer-by-layer with an alternating 0–90° stacking pattern to ensure high structural precision. Immediately after printing, the scaffolds were crosslinked in 3% sterile $CaCl_2$ solution (Sigma, USA) for 5 min,[41] rinsed with sterile phosphate-buffered saline (PBS), and prepared for subsequent experiments.

2.4. Surface morphology analysis

The microstructure and surface morphology of the 3D-bioprinted Gel–Alg hydrogel scaffolds were examined using field emission scanning electron microscopy (SEM) (Jeol, Japan). Briefly, the scaffolds were freeze-dried under a vacuum for 24 h to preserve their structural integrity. The dried samples were then fractured to obtain cross-sectional views for microscopic analysis. To improve electron conductivity, the surfaces were treated with a gold jet machine (Jeol, Japan). Imaging was performed at an acceleration voltage of 10 kV.

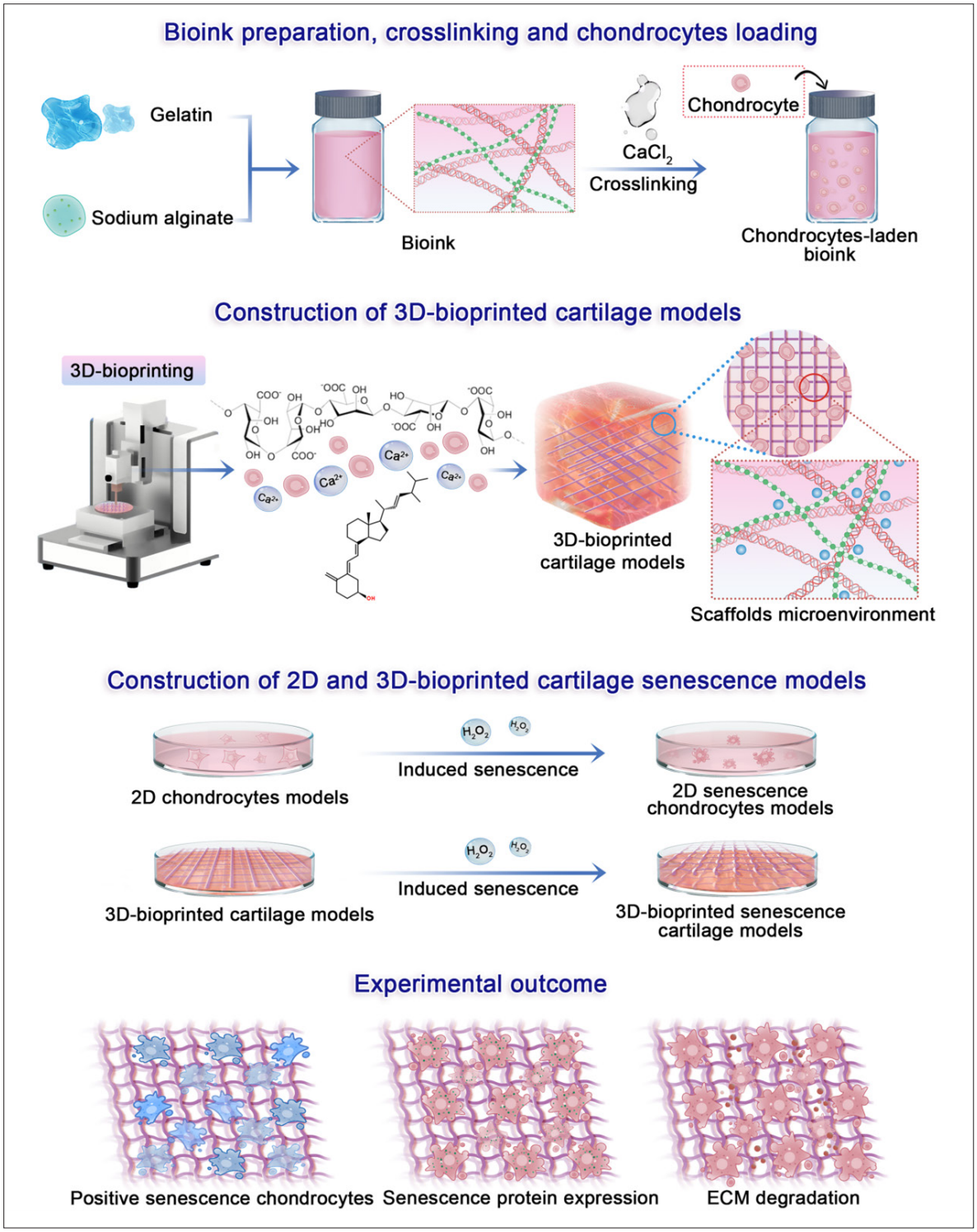

Figure 1. Schematic demonstration of 3D-bioprinted cartilage models that can be externally induced using H_2O_2 to build cartilage senescence models and the construction of 2D chondrocyte senescence models. Abbreviation: ECM, extracellular matrix.

2.5. Mechanical strength analysis

To evaluate the mechanical properties of the 3D-bioprinted Gel–Alg hydrogel scaffolds, a universal testing machine (Instron, USA) was used. Briefly, the scaffolds were fabricated into 3D-bioprinted rectangular columns with dimensions of 8 × 8 × 8 mm and subjected to uniaxial compression at a rate of 1 mm/min until 50% strain was reached. The compressive Young's modulus was calculated from the linear region of the initial 10% of the stress–strain curve, while toughness was determined by measuring the area under the curve. All measurements were performed in triplicate.

2.6. Water absorption and degradation behavior

The swelling and water absorption properties of the 3D-bioprinted hydrogel scaffolds were evaluated using the conventional weighing method. Briefly, the scaffolds were freeze-dried to obtain their initial dry weight (W0) and then immersed in 2 mL of PBS. The wet samples were maintained in a 37°C incubator. At specific time intervals (100, 200, 300, 400, and 500 min), the scaffolds were removed, and excess water was blotted with filter paper. The wet weight (Wt) of each scaffold was recorded. The percentage of swelling rate and water content was calculated using **Equation I**:

$$\text{Water content}\ (\%) = \frac{(\text{Wt} - \text{W0})}{\text{W0}} \times 100\% \qquad \text{(I)}$$

where W0 is the initial dry weight, and Wt is the wet weight of each sample at a different time point. Each sample was independently run in triplicate.

The *in vitro* degradation behavior of the 3D-bioprinted hydrogel scaffolds was evaluated using a gravimetric analysis method. Briefly, the scaffolds were freeze-dried, and their initial dry weight (W0) was recorded. The scaffolds were immersed in PBS (pH 7.4) containing type II collagenase (COL2) and maintained in a shaker at 37°C with a shaking speed of 40 rpm. At specific time points (0, 2, 4, 6, 8, and 10 h), the samples were removed, dried, and weighed again (Wt). Each experiment was performed in triplicate to ensure the reliability of the results. The degradation rate of the scaffolds was calculated using **Equation II**:

$$\text{Degradation rate}\ (\%) = \frac{(\text{W0} - \text{Wt})}{\text{W0}} \times 100\% \qquad \text{(II)}$$

where W0 is the initial weight, and Wt is the measured weight at each time period. Each sample was independently run in triplicate.

2.7. Porosity test

The porosity of the 3D-bioprinted Gel–Alg hydrogel scaffolds was measured using the ethanol displacement method. Briefly, the scaffolds were freeze-dried to remove internal moisture. The dried scaffolds were accurately weighed (W0). Subsequently, the dimensions of the freeze-dried scaffolds were measured using a vernier caliper to calculate their theoretical volume (V0). The dried scaffolds were then placed in a test tube pre-filled with ethanol, ensuring complete immersion of the scaffolds. The tube was sealed and placed under a vacuum for 2 h to allow ethanol to fully infiltrate the pores of the scaffolds.[42] The process was monitored continuously until no bubbles were observed, indicating complete displacement. After removal, the scaffolds were gently blotted with filter paper to remove excess ethanol and immediately weighed (W1). The experiment was repeated three times independently to ensure data reliability. The porosity of the scaffolds was calculated using **Equation III**:

$$\text{Porosity}(\%) = \frac{(\text{W1} - \text{W0})}{\rho\,\text{V0}} \times 100\% \qquad \text{(III)}$$

where W0 is the initial weight, W1 is the measured weight at each time period, ρ is the density of ethanol, and V0 is the scaffold volume.

2.8. Isolation and amplification of articular chondrocytes

All four-week-old male Sprague-Dawley (SD) rats were provided by the Department of Laboratory Animals of the Zhejiang Province Experimental Animal Center. The study strictly adhered to the guidelines of the Institutional Animal Care and Use Committee of Hangzhou Institute of Medicine Chinese Academy of Sciences and was in accordance with the principles of the Declaration of Helsinki for the care and use of animals. After anesthesia, four-week-old male SD rats were euthanized, and the carcasses were disinfected by immersion in 75% ethanol for 20 min. The skin was removed, and the lumbar spine was isolated, discarding the tail and ankles while preserving the hip and knee joints. The joints were then rinsed with 75% ethanol. Under aseptic conditions, the joint capsule was opened, and the surrounding muscle tissue was carefully removed. The meniscus was excised to expose the articular cartilage. Cartilage from the knee joint and femoral head was harvested and rinsed with PBS. The tissue was transferred into a trypsin–EDTA solution (Sigma, USA) and digested on a shaker at 37°C and 85 rpm for 30 min. Following digestion, the samples were washed with PBS and transferred to a centrifuge tube containing 0.2% COL2 (Sigma, USA) for further digestion at 37°C for 4 h under

agitation.[43] When visible cartilage fragments were reduced, an equal volume of Dulbecco's Modified Eagle Medium (DMEM) (Gibco, USA), supplemented with 10% fetal bovine serum (FBS) (Bio Channel, China), was added to terminate the enzymatic reaction. The mixture was centrifuged at 1200 rpm for 10 min, the supernatant was discarded, and the cell pellet was collected. The cells were seeded in DMEM containing 10% FBS and 1% penicillin–streptomycin (Gibco, China). AC growth was monitored under a microscope, and the culture medium was replaced every 2–3 days. When the primary ACs reached 80–90% confluence, they were used for subsequent staining identification and 3D bioprinting of cartilage models.

2.9. Identification of articular chondrocytes

2.9.1. Safranin O staining

The ACs were rinsed three times with PBS to remove the residual culture medium. Subsequently, 4% paraformaldehyde (PFA) was added, and the cells were fixed at room temperature for 20 min. After fixation, the samples were washed three times with PBS for 5 min each to remove the fixative. The fixed samples were then immersed in Safranin O staining solution (Suzhou Haixing Biosciences, China) and incubated at room temperature for 10 min. Following staining, the samples were thoroughly rinsed with distilled water to remove excess dye. Dehydration was performed using a graded ethanol series (70, 90, and 100%) for 2 min each. Finally, the stained samples were observed under an optical microscope.

2.9.2. Alcian Blue staining

The ACs were rinsed three times with PBS to remove the residual culture medium. Subsequently, 4% PFA was added, and the cells were fixed at room temperature for 20 min. The fixed samples were then immersed in Alcian Blue staining solution (Suzhou Haixing Biosciences, China) and incubated at room temperature for 30 min. Following staining, the samples were thoroughly rinsed with distilled water to remove excess dye. Dehydration was performed using a graded ethanol series (70, 90, and 100%) for 2 min each. Finally, the stained samples were observed under an optical microscope.

2.9.3. Toluidine Blue staining

The ACs were rinsed three times with PBS to remove the residual culture medium. Subsequently, the cells were fixed with 4% PFA at room temperature for 20 min. A 0.1% Toluidine Blue staining solution (pH 2.5–3.0) (Suzhou Haixing Biosciences, China) was added to cover the samples, followed by incubation at room temperature for 10–15 min. The samples were then quickly immersed in a 0.1% acetic acid solution for 5–10 s for differentiation and rinsed three times with distilled water for 1 min each. Dehydration was performed using a graded ethanol series (70, 90, and 100%) for 2 min each. Finally, the stained samples were observed under an optical microscope.

2.10. Construction of 3D-bioprinted cartilage models

The primary ACs of SD rats were selected as seed cells, and three different concentration ratios of Gel–Alg natural polymer hydrogels were used as scaffolds to construct cartilage models using 3D bioprinting technology. Based on preliminary research, the optimal Gel–Alg ratios were determined to be 7:3, 8:2, and 9:1. The bioinks were thoroughly mixed on a shaker at 60°C. For each formulation, 500 μL of bioink was transferred to a printing cartridge, and 50 μL of ACs suspension was immediately added to the cartridge and mixed with the hydrogel. Printing was performed on a 4°C 3D printer platform, with the filament diameter set to 200 μm, the number of layers set to four, and the printing spacing set to 0.22 mm. Printing parameters, including extrusion pressure (0.25, 0.3, 0.35, and 0.4 Mpa), printing speed (5, 8, 10, and 12 mm/s), and printing nozzle temperature (16, 18, and 20°C), were dynamically adjusted during the process to optimize the printing outcome. After printing, the cartilage models were crosslinked in a sterile 3% $CaCl_2$ solution for 3 min and rinsed with sterile PBS to remove residual crosslinking agents. The cartilage model was then transferred to DMEM culture and placed in a cell culture chamber at 37 °C and 5% CO_2 to support cartilage tissue growth.

2.11. Live/dead cell assay

The potential damage to AC viability during the 3D bioprinting process was assessed using live/dead staining assay. After printing, the constructs were cultured in 10% FBS DMEM for 1 day. Prior to the experiment, the culture medium was removed, and the constructs were rinsed with sterile PBS. The constructs were then incubated for 15 min in an assay buffer solution containing 4 μM calcein AM and 4.5 μM propidium iodide (Biosharp, China). After staining, the constructs were rinsed again with sterile PBS. A fluorescent microscope (Nikon, Japan) was used for observation at a wavelength of 490 ± 10 nm. Cell viability was quantified using ImageJ software (Media Cybernetics, USA).

2.12. Cell counting kit-8 assay

The proliferation activity of ACs within the hydrogel scaffolds was evaluated using the cell counting kit-8 (CCK-8) assay. After printing, the constructs were cultured in 10% FBS DMEM for 1 day. On days 1, 4, and 7, the medium was replaced with fresh medium containing 10% CCK-8 (Shenzhen JHHS Biotech, China) and incubated at

37 °C for 2 h. Subsequently, the absorbance at 450 nm was measured using a microplate reader (Tecan, Switzerland). Ten samples from each group were included for statistical analysis.

2.13. Extracellular matrix secretion assay

The secretion of extracellular matrix (ECM) (proteoglycans and glycosaminoglycans [GAGs]) by ACs in 3D-bioprinted cartilage models was detected using Safranin O and Toluidine Blue staining (Suzhou Haixing Biosciences, China) to evaluate the formation and function of cartilage tissue. After printing, the constructs were cultured in 10% FBS DMEM for 5 days. Prior to the experiment, the 3D-bioprinted cartilage models were rinsed with sterile PBS to remove residual culture medium. Subsequently, the samples were fixed with 4% PFA at room temperature for 1 h and washed with sterile PBS to remove the fixative. The fixed samples were then immersed in Safranin O and Toluidine Blue staining solutions, respectively, and incubated at room temperature for 40 min. After staining, the samples were thoroughly rinsed with distilled water to remove excess dye. Dehydration was performed using a graded ethanol series (70, 90, and 100%). Finally, the stained samples were observed under an optical microscope (Olympus, Japan).

2.14. Construction of 2D articular chondrocyte senescence models

The effects of oxidative stress on 2D AC models and 2D AC senescence models were established using H_2O_2 induction. A 3% H_2O_2 stock solution (Biosharp, China) was diluted with a serum-free medium by volume to prepare H_2O_2 solutions at concentrations of 0 (control group), 100, 300, 500, and 700 μM. These were used for constructing the 2D AC senescence models. The optimal H_2O_2 concentration for constructing the senescence model was determined through β-galactosidase staining (Biosharp, China), and this concentration was subsequently used for constructing the 3D-bioprinted cartilage senescence models. Briefly, the 3% H_2O_2 stock solution was sequentially diluted to the control group, 100, 300, 500, and 700 μM using a gradient dilution method. Subsequently, the 2D AC models were rinsed with sterile PBS to remove the residual culture medium on the surface. Finally, the 2D AC models were cultured with different concentrations of H_2O_2 for 2, 6, and 12 h to determine the optimal concentration and time for inducing the senescence model. After the induction of the senescence model was completed, the H_2O_2 diluent was removed, and the models were rinsed with sterile PBS for subsequent detection.

2.15. β-galactosidase staining analysis

The β-galactosidase staining was used to determine the optimal H_2O_2 concentration and induction time for constructing the 2D AC senescence model, and the optimal conditions were applied to construct the 3D-bioprinted cartilage senescence model. Briefly, the H_2O_2 diluent was removed, and the samples were rinsed with PBS. Then, 1 mL of β-galactosidase staining fixative (Beijing LABLEAD Inc, China) was added, and the cells were fixed at room temperature for at least 15 min. Subsequently, the fixative was removed, and the samples were rinsed with PBS. Next, 2 mL of working staining solution containing X-Gal substrate was added, and the samples were incubated overnight at 37°C. Finally, β-galactosidase activity was observed using a fluorescence microscope, and quantitative analysis was performed using ImageJ software.

2.16. Construction of 3D-bioprinted cartilage senescence models

We constructed the 3D-bioprinted cartilage senescence models using the optimal H_2O_2 concentration and induction time (determined previously in **Section 2.15**). Briefly, the complete medium was removed, and the samples were rinsed with sterile PBS. Subsequently, 500 μM H_2O_2 diluent was added, and the samples were cultured for 2 h. Finally, the H_2O_2 diluent was removed, and the samples were rinsed with PBS for subsequent detection.

2.17. Cell viability analysis of senescence models

The cell viability of 2D AC senescence models and 3D-bioprinted cartilage senescence models was evaluated using the CCK-8 assay to compare the proliferation of cells in both models under senescence conditions. Briefly, the 2D AC senescence models and 3D-bioprinted cartilage senescence models were transferred into 24-well plates and cultured in a complete medium. After 24 h of culture, the complete medium was removed, and the samples were rinsed with sterile PBS. The medium was then replaced with fresh medium containing 10% CCK-8 (Biosharp, China) and incubated at 37°C for 2 h. Subsequently, the absorbance at 450 nm was measured using a microplate reader (Tecan, Switzerland). Ten samples from each group were included for statistical analysis.

2.18. Western blot analysis

The differences in senescence-related protein expression between 2D AC senescence models and 3D-bioprinted cartilage senescence models were explored using Western blot. Briefly, total protein was extracted from the 2D AC senescence models and 3D-bioprinted cartilage senescence models using radioimmunoprecipitation lysis buffer (Thermo Fisher, China) supplemented with 1% protease inhibitor and phosphatase inhibitor (Thermo Fisher, China). The protein concentration was determined using the bicinchoninic acid assay (Thermo Fisher, China). Equal amounts of protein were electrophoresed by sodium dodecyl sulfate–polyacrylamide gel electrophoresis and

transferred to polyvinylidene fluoride (PVDF) blotting membranes (Millipore, USA). The membranes were incubated with Fast Blocking Buffer (Epizyme, China) at room temperature for 15 min and then incubated overnight at 4°C with primary antibodies against p16 (1:600) (Biosharp, China), p21 (1:800) (Biosharp, China), and β-actin (1:1000) (Hangzhou UpingBio Technology, China). The membranes were washed with DAPI (4',6-Diamidino-2-phenylindole) TBST (Tris-buffered saline with Tween 20) (Thermo Fisher, China) and incubated with horseradish peroxidase-coupled secondary antibodies (1:2000) (Jackson, USA) at room temperature for 1 h. After washing the PVDF membranes again, the bands were visualized using an enhanced chemiluminescence solution (Biosharp, China) and a Gel Analysis System (Cytiva, USA).

2.19. Immunofluorescence

The expression differences in 2D AC senescence models and 3D-bioprinted cartilage senescence models were observed using immunofluorescence staining to evaluate the molecular characteristics of both models under senescence conditions. Briefly, the 2D AC senescence models and 3D-bioprinted cartilage senescence models were rinsed three times with PBS to remove the residual culture medium. Subsequently, 4% PFA was added, and the samples were fixed at room temperature for 20 min. After fixation, the samples were washed three times with PBS for 5 min each to remove the fixative. Then, 0.1% Triton X-100 (Biosharp, China) was added, and the samples were permeabilized at room temperature for 10 min to enhance antibody penetration. The samples were rinsed three times with PBS for 5 min each. Next, a 5% bovine serum albumin solution (Thermo Fisher, China) was added, and the samples were blocked at room temperature for 30 min to reduce non-specific binding. After blocking, the samples were rinsed once with PBS to remove the blocking solution. Diluted primary antibodies p16 (1:300) (Biosharp, China), p21 (1:300) (Biosharp, China), and COL2 (1:300) (Thermo Fisher, China) were added, and the samples were incubated overnight at 4°C. The samples were then washed three times with PBS for 5 min each to remove unbound primary antibodies. Fluorescently labeled secondary antibodies Alexa Fluor 488 (1:500) (Thermo Fisher, China) and Alexa Fluor 594 (1:500) (Thermo Fisher, China) were added, and the samples were incubated at room temperature in the dark for 1 h. After incubation, the samples were washed three times with PBS for 5 min each to remove unbound secondary antibodies. DAPI solution (1:1000) (Thermo Fisher, China) was added, and the samples were incubated at room temperature in the dark for 5 min to stain the nuclei. The samples were rinsed three times with PBS for 5 min each. Finally, the samples were observed under a fluorescence microscope, and the fluorescence signals of p16, p21, and COL2 were detected using different excitation wavelengths (488 and 594 nm). Images were captured and quantitatively analyzed using ImageJ analysis software.

2.20. Statistical analysis

All data were processed and analyzed using OriginPro 2022 (OriginLab Corporation, USA). Statistical significance was determined using one-way or two-way analysis of variance, followed by Tukey's post-hoc test for multiple comparisons. All the experiments were performed in triplicate, and the results were presented as the mean ± standard deviation. The statistical significance was set as: ns, no significant; $^{*}p < 0.05$; $^{**}p < 0.01$; $^{***}p < 0.001$; and $^{****}p < 0.0001$.

3. Results and discussion

3.1. 3D bioprinting and characterization of gelatin and sodium alginate hydrogel scaffolds

Three different concentration ratios of Gel–Alg were prepared (Figure 2B). The bioink should exhibit high viscoelasticity under high shear stress to increase printability. Optimal viscoelastic properties ensure stable bioink extrusion through 3D bioprinting nozzles while maintaining structural integrity.[44,45] Alg is a naturally occurring block copolymer composed of polymer chains of β-D-mannuronic acid (M) and α-L-guluronic acid (G). It is an ideal biomaterial for bioprinting hydrogels, as its printability can be readily tuned by adjusting the polymer density and crosslinking with $CaCl_2$.[46–48] Alg alone lacks mammalian cell adhesion ligands, but incorporating Gel can promote cell adhesion and differentiation, as well as adjust the viscosity of the hydrogel.[49] Thus, this study chose the Gel–Alg bioink with optimal viscoelastic properties and printability. At a shear rate of 200 s^{-1}, the viscosity of the 7 Gel–3 Alg bioink was measured at 5.30 ± 0.73 Pa·s, whereas the viscosities of 8 Gel–2 Alg and 9 Gel–1 Alg bioinks were 2.27 ± 0.30 Pa·s and 1.95 ± 0.36 Pa·s, respectively (Figure 2D). These findings indicate that 7 Gel–3 Alg exhibited optimal shear-thinning behavior, making it highly suitable for extrusion-based 3D bioprinting. In the low strain range (0.01–10%), G' and G" were relatively constant. However, 7 Gel–3 Alg demonstrated G' of 7830 ± 8.54 Pa and G" of 948 ± 0.41 Pa, higher than those of 8 Gel–2 Alg (G' = 2113 ± 0.61 Pa; G" = 216 ± 0.21 Pa) and 9 Gel–1 Alg (G' = 1542 ± 0.89 Pa; G" = 66 ± 0.86 Pa) (Figure 2E), indicating superior linear viscoelastic properties of 7 Gel–3 Alg.

Employing a layer-by-layer 0–90° alternating stacking strategy, precise Gel–Alg hydrogel scaffolds were fabricated. After 3D bioprinting, the scaffolds underwent $CaCl_2$ crosslinking to enhance mechanical properties.[50–52]

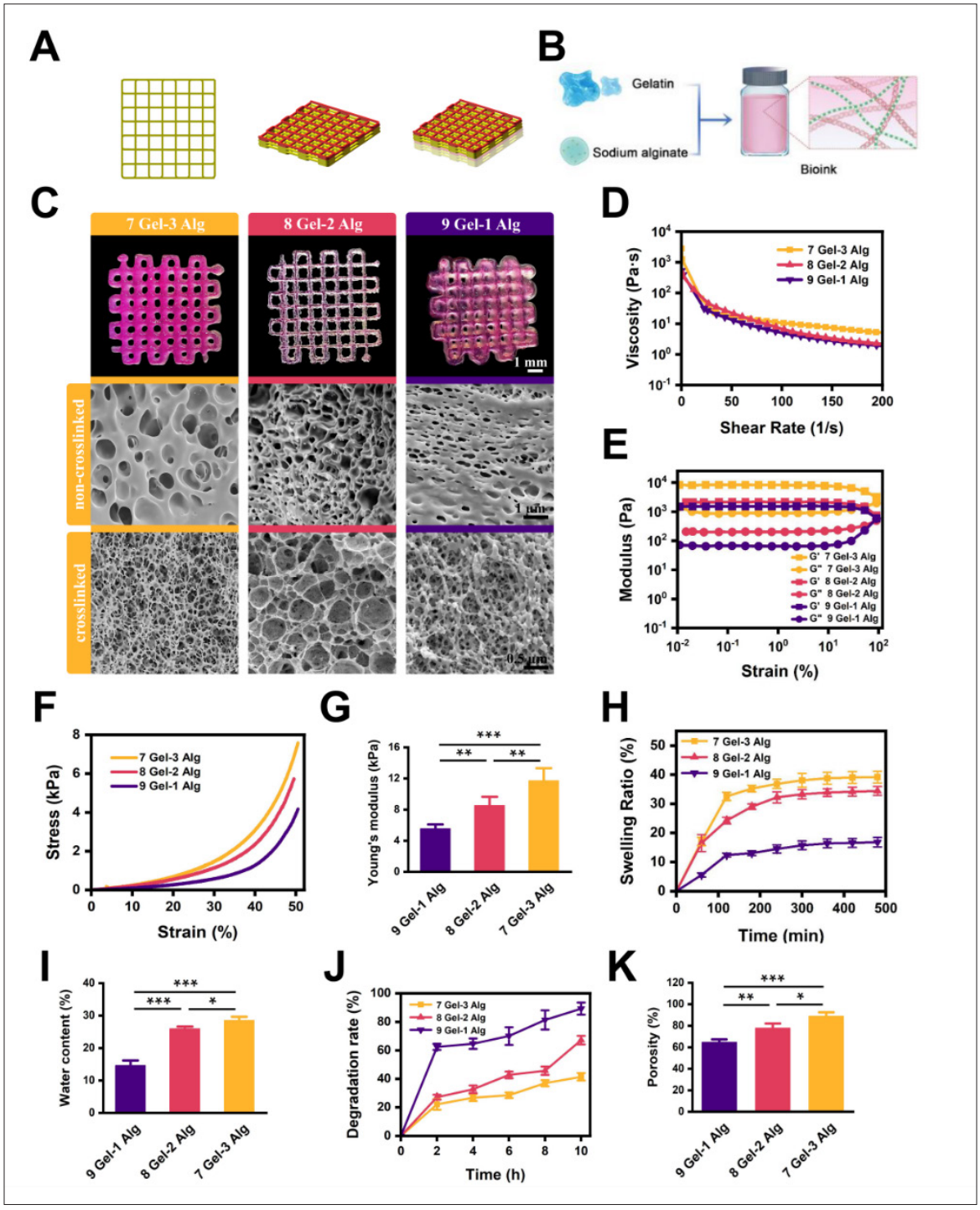

Figure 2. Construction and characterization of a 3D-bioprinted hydrogel scaffold. (A) Single-layer and multi-layer models of 3D-bioprinted hydrogel scaffolds. (B) Schematic illustration of natural bioink preparation. (C) Structural profiles of the printed Gel–Alg hydrogel scaffolds; SEM images of non-crosslinked and crosslinked Gel–Alg hydrogel scaffolds. (D and E) The viscosity (D) and modulus (E) of the natural bioink. (F) Stress–strain curves of the Gel–Alg hydrogel scaffolds. (G) Statistical Young's modulus of the Gel–Alg scaffolds. (H and I) Swelling performance (H) and water content (I) of the Gel–Alg hydrogel scaffolds. (J) *In vitro* degradation performance of the scaffolds. (K) Porosity of the Gel–Alg hydrogel scaffolds. All statistical data are represented as mean ± standard deviation ($n = 3$; $^{*}p < 0.05$, $^{**}p < 0.01$, $^{***}p < 0.001$). Scale bar: 1 mm (C). Abbreviations: ACs, articular chondrocytes; Alg, alginate; GAGs, glycosaminoglycans; Gel, gelatin; SEM, scanning electron microscopy; sGAGs, sulfated glycosaminoglycans.

However, printing smaller models with a diameter of less than 10 mm was challenging due to the limitations of extruded 3D printing technology.[53] Although laser-assisted bioprinting has higher precision and can be used to construct Gel–Alg hydrogel scaffolds, it is challenging to maintain their bioactivity. This study prioritized physical crosslinking for improved biocompatibility, avoiding cytotoxicity associated with UV-initiated chemical crosslinking.[54] To eliminate potential mineral deposits from residual calcium ions on the scaffold surface, constructs were rinsed with sterile PBS. Figure 2C displays the structural profiles of Gel–Alg hydrogel scaffolds at three different concentration ratios. Furthermore, SEM images reveal microstructures of the scaffolds in both crosslinked and non-crosslinked states. Figure 2C also indicates that the 3D-bioprinted Gel–Alg scaffolds maintained a stable multi-layered grid structure with tightly stacked layers and an interconnected porous network suitable for AC growth. The pore sizes of the 7 Gel–3 Alg, 8 Gel–2 Alg, and 9 Gel–1 Alg scaffolds are 5.47 ± 0.87 μm, 2.29 ± 0.048 μm, and 1.18 ± 0.061 μm, respectively. High-magnification observations revealed dense pore walls formed by Alg crosslinking intertwined with Gel-derived microfiber structures, providing rough surfaces that enhance cell adhesion and increase specific surface area. The uniformity of printed fiber diameters and seamless interlayer fusion suggest that structural integrity was maintained through optimized printing parameters.

The mechanical strength was evaluated to confirm the stability of the polymer network following physical crosslinking, and the stress–strain curves were plotted (Figure 2F). Based on previous research, a higher concentration of Gel–Alg hydrogels ionic-crosslinked with $CaCl_2$ significantly enhanced the mechanical strength of the scaffolds.[55] Therefore, according to Figure 2G, Young's modulus of the 7 Gel–3 Alg scaffold is 11.7 ± 1.66 kPa, significantly higher than the values for 8 Gel–2 Alg and 9 Gel–1 Alg (8.52 ± 6.67 kPa and 5.56 ± 2.23 kPa, respectively). This suggests superior stiffness under load, crucial for maintaining structural integrity and performance in physiological conditions.

The swelling behavior was assessed to evaluate the hydrophilicity of the Gel–Alg scaffolds, which is crucial for maintaining a hydrated microenvironment conducive to nutrient diffusion, cellular viability, and growth.[56] All scaffolds demonstrated rapid water absorption in the first 120 min, followed by a deceleration in absorption from 120 to 240 min, with equilibrium swelling achieved after 240 min. The equilibrium swelling ratios of 8 Gel–2 Alg and 9 Gel–1 Alg were 34.4 ± 1.48% and 16.8 ± 1.48%, significantly lower than that of 7 Gel–3 Alg (39.2 ± 3.22%). This difference is attributed to the denser structure of 7 Gel–3 Alg, as supported by SEM analysis (Figure 2H).

To further determine the water content of Gel–Alg hydrogel scaffolds at swelling equilibrium in deionized water, gravimetric analysis was conducted. The results revealed similar equilibrium water contents of 7 Gel–3 Alg and 8 Gel–2Alg scaffolds at approximately 30%, reflecting similar hydrophilic properties (Figure 2I). This hydrophilicity is likely due to hydrophilic groups (–NH2, –COOH, and –OH) within the molecular chains of Gel and Alg components.[57] Water absorption and swelling are critical for retaining structural integrity and cellular microenvironments. Thus, achieving adequate swelling capacity is essential for optimal scaffold performance.

The degradation behavior was evaluated in the COL2 solution to assess scaffold stability. Following 2 h of incubation, 8 Gel–2 Alg and 9 Gel–1 Alg scaffolds exhibited significant mass loss, with degradation rates of 67.2 ± 2.90% and 89.2 ± 4.76% after 10 h, respectively. This observation suggests that increased Gel content accelerates degradation. In contrast, the 7 Gel–3 Alg scaffold exhibited a degradation rate of 41.4 ± 2.86% after 10 h, indicating that Alg enhances degradation resistance proportionally with its concentration in the composite (Figure 2J).

The porosity of the scaffolds was further evaluated, and the porosity of the 7 Gel–3 Alg, 8 Gel–2 Alg, and 9 Gel–1 Alg scaffolds was 88.9 ± 3.67%, 77.91 ± 4.66%, and 64.63 ± 2.48%, respectively. SEM comparisons attributed the superior porosity of 7 Gel–3 Alg to its structured pore network with multi-scale pore distribution, fostering efficient nutrient and fluid transport to create an optimal environment for cellular adhesion and proliferation (Figure 2K).

3.2. *In vitro* biocompatibility and cartilage extracellular matrix secretion by gelatin and sodium alginate hydrogel scaffolds

ACs isolated from the knee joints of four-week-old male SD rats were cultured for integration with 3D-bioprinted Gel–Alg hydrogel scaffolds (Figure 3A). After isolation and expansion, primary ACs were stained with Safranin O, Alcian Blue (pH 1.0), and Toluidine Blue to confirm ECM synthesis capacity. Studies have demonstrated that the Gel component provides a scaffold that mimics the ECM of ACs, while the Alg component imparts mechanical properties similar to those of cartilage. Gel–Alg promotes the secretion of AC ECM, manifesting as increased cell viability, higher levels of collagen II and proteoglycan expression, and elevated GAG content.[58,59] Safranin O

staining indicated a proteoglycan-rich matrix, while Alcian Blue (under acidic conditions) identified sulfated glycosaminoglycans (sGAGs) through distinct cyanophilic interactions. Toluidine Blue confirmed the presence of anionic GAGs via γ-metachromatic purple coloration (Figure 3B). The morphological assessment revealed cells adopting rounded or polygonal shapes with pericellular lacunae formation, establishing a baseline for evaluating 3D hydrogel scaffolds in cartilage ECM homeostasis.

In vitro biocompatibility and cellular viability were validated through CCK-8 and live/dead assays. Prior studies

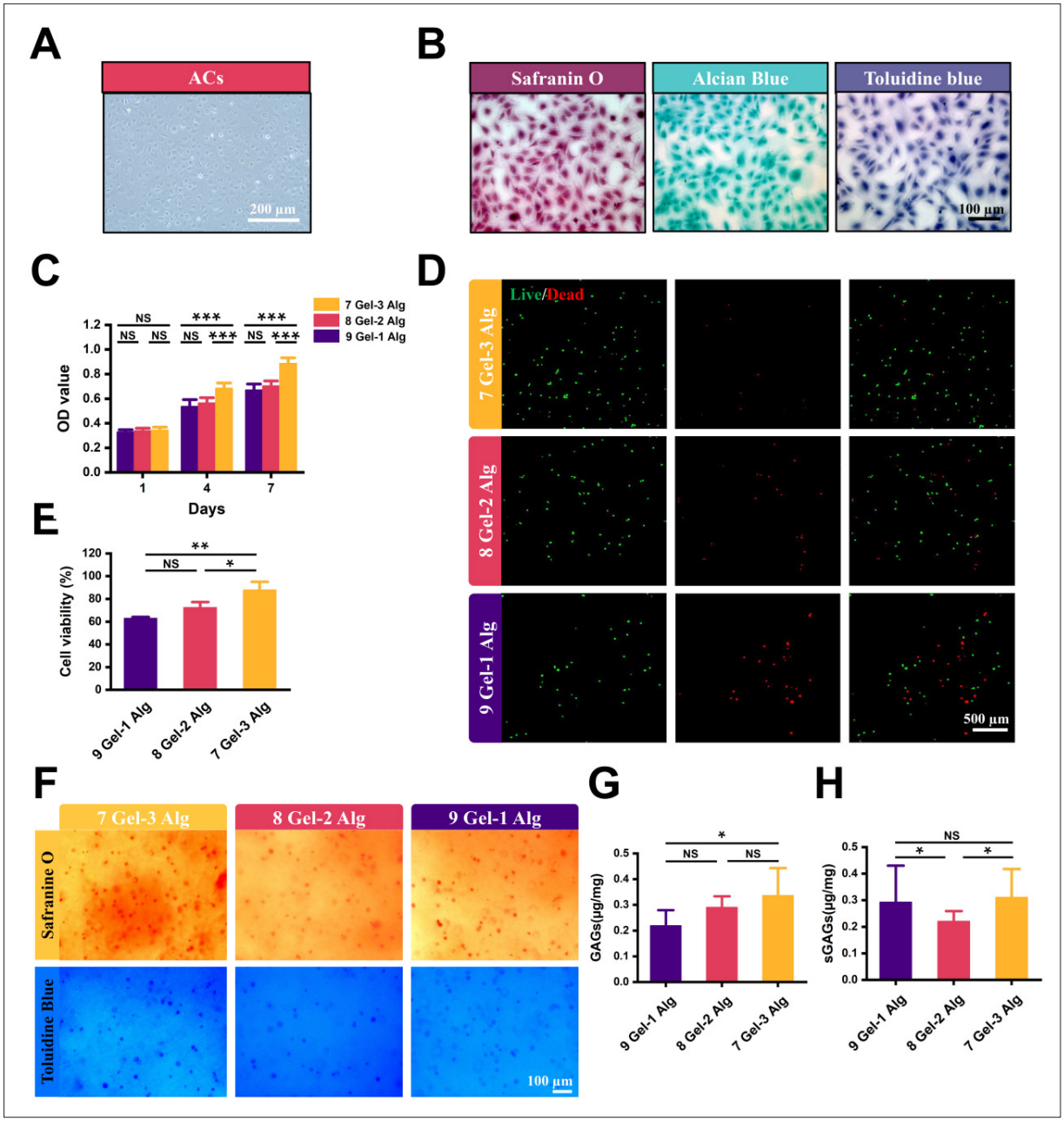

Figure 3. The 3D-bioprinted Gel–Alg hydrogel scaffolds support the survival, proliferation, and extracellular matrix secretion of the embedded cells. (A and B) The morphology (A) and staining (Safranin O, Alcian Blue, and Toluidine Blue) (B) of primary ACs. (C) Quantitative analysis of the AC proliferation rate *in vitro* 2D culture. (D) Cell viability determined by live/dead staining. (E) Quantification analysis of AC viability. (F) Safranin O and Toluidine Blue staining of 3D-bioprinted cartilage model. (G and H) Quantification analysis of GAGs (G) and sGAGs (H). All statistical data are represented as mean ± standard deviation ($n = 5$; $^{*}p < 0.05$, $^{**}p < 0.01$, $^{***}p < 0.001$). Scale bars: 100, 200, and 500 μm. Abbreviations: ACs, articular chondrocytes; Alg, alginate; GAGs, glycosaminoglycans; Gel, gelatin; NS, non-significant; OD, optical density; sGAGs, sulfated glycosaminoglycans.

indicate that decreased cell viability primarily results from high shear stress at the nozzle tip during printing.[60–62] In this study, 7 Gel–3 Alg hydrogel scaffolds exhibited the highest absorbance values compared to 8 Gel–2 Alg and 9 Gel–1 Alg (Figure 3C). These findings confirm that 3D-bioprinted 7 Gel–3 Alg scaffolds significantly enhance cellular viability and proliferation. Live/dead assays on AC-laden scaffolds after 1 day displayed cell viabilities of 87.9 ± 7.60%, 72.4 ± 5.03%, and 62.9 ± 0.83% for 7 Gel–3 Alg, 8 Gel–2 Alg, and 9 Gel–1 Alg, respectively (Figure 3D and E). After 7 days, AC-laden Gel–Alg hydrogel scaffolds stained with Safranin O and Toluidine Blue revealed the spatial distribution of negatively charged GAGs, proteoglycans, and sGAGs, enabling quantitative evaluation of tissue maturation (Figure 3F). The quantitative analysis results indicate that the 7 Gel–3 Alg scaffolds had higher GAG and sGAG contents compared to the 8 Gel–2 Alg and 9 Gel–1 Alg scaffolds (Figure 3G and H).

3.3. Development and functional characterization of a 2D chondrocytes senescence model

Approximately 3 × 10^6 ACs were exposed to H_2O_2 at concentrations of 0 (control), 100, 300, 500, and 700 μM for 2, 6, and 12 h to simulate oxidative stress-induced senescence and assessed via SA-β-galactosidase activity assays (Figure 4A). Previous studies have reported that during the process of ACs senescence, SA-β-gal activity was observed, involving senescence-associated markers (p16 and p21).[63,64] At 2 h, the SA-β-galactosidase-stained senescent cell rates were 4.67 ± 1.52%, 21.0 ± 3.61%, 58.0 ± 10.15%, 85.0 ± 3.61%, and 57.33 ± 6.11% in the control, 100, 300, 500, and 700 μM H_2O_2 groups, respectively (Figure 4B and C). Compared to the control group, the 500 μM H_2O_2 group achieved peak senescence ($p < 0.001$), while extensive apoptosis was observed at 700 μM. At 6 h, the SA-β-galactosidase-positive cell rates were 6.33 ± 1.53%, 35.33 ± 8.33%, 75.0 ± 3.00%, 50.33 ±

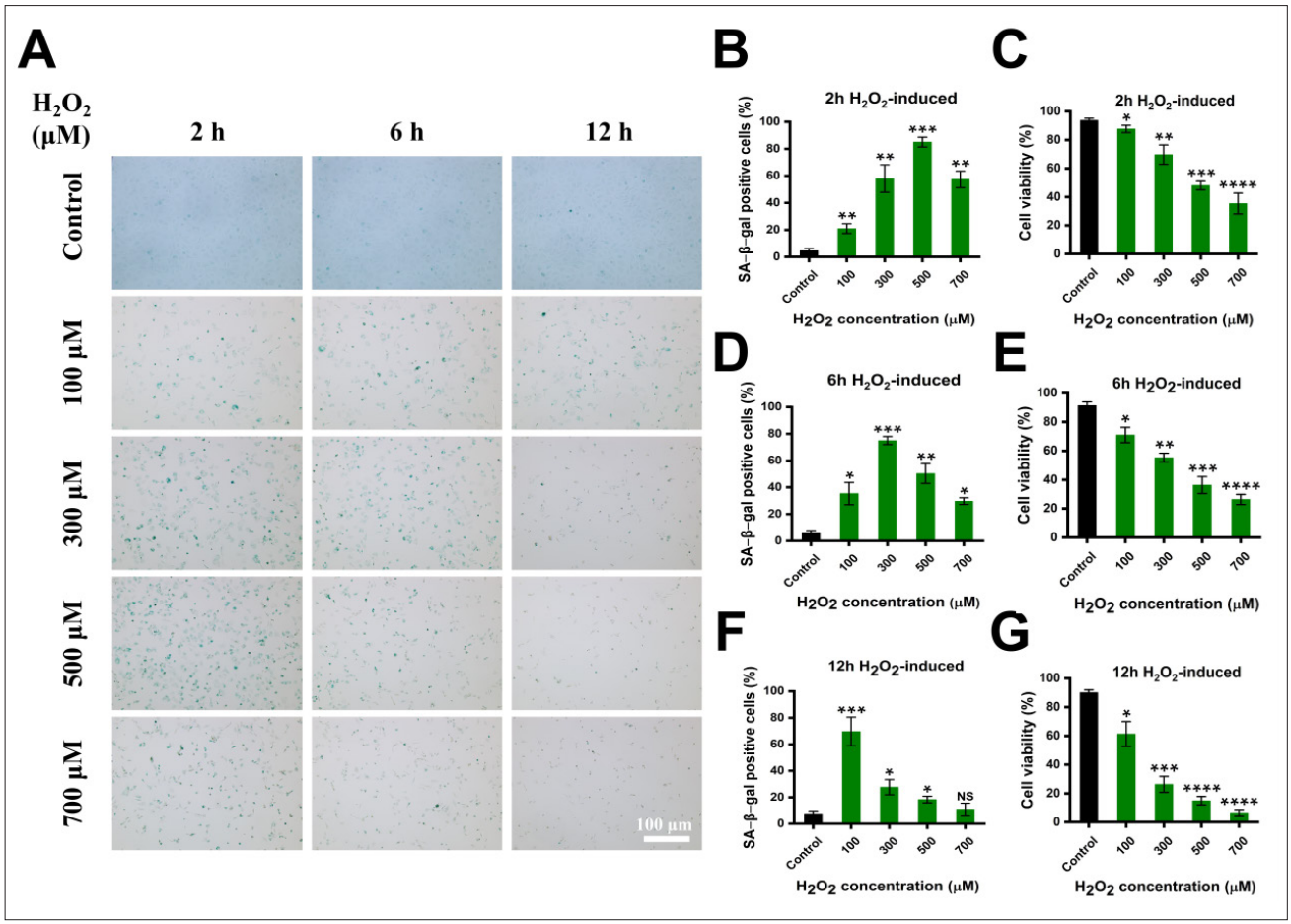

Figure 4. Construction of 2D AC senescence models. (A) β-Galactosidase staining of 2D ACs. (B–G) Quantitative analysis of the rate of AC senescence (B, D, and F) and viability (C, E, and F) following H_2O_2 induction at 2 (B and C), 6 (D and E), and 12 h (F and G). All statistical data are represented as mean ± standard deviation ($n = 3$; $^*p < 0.05$, $^{**}p < 0.01$, $^{***}p < 0.001$). Scale bar: 100 μm (A). Abbreviations: AC, articular chondrocyte.

7.37%, and 29.67 ± 2.52%, respectively (Figure 4D and E). Compared to the control group, the 300 μM H_2O_2 group exhibited significant senescence ($p < 0.001$), with apoptosis observed at higher concentrations. At 12 h, the SA-β-galactosidase-positive cell rates were 7.67 ± 2.08%, 69.67 ± 10.79%, 27.67 ± 5.69%, 18.33 ± 2.52%, and 11.0 ± 4.58%, respectively (Figure 4F and G). Compared to the control group, the 100 μM H_2O_2 group reached peak senescence ($p < 0.001$), while apoptosis was evident at higher concentrations.

These findings suggest that high-concentration oxidative stress overwhelms cellular regulatory mechanisms, causing macromolecular lesions and ultimately disrupting redox homeostasis.[65–67] The optimal conditions for inducing AC senescence were identified as a 2-h exposure to 500 μM H_2O_2, resulting in 85.0 ± 3.61% SA-β-gal-positive cells without significant apoptosis ($p < 0.001$ vs. control); and the 500 μM H_2O_2 concentration was applied to induce senescence in 3D-bioprinted cartilage models. Prolonged exposure (6 and 12 h) induced significant apoptosis (50.33–29.67% viable cells), making these conditions unsuitable for further studies.

The expression levels of senescence-associated proteins p21 and p16 were assessed through Western blot analysis and immunofluorescence, followed by semi-quantitative analysis using ImageJ software. The senescence phenotype is not limited to cell cycle arrest; senescent cells are metabolically active and exhibit changes in protein expression and secretion, leading to Senescence-Associated Secretory Phenotype development.[68] Results indicated significant H_2O_2-induced effects on AC senescence. As illustrated in Figure 5A, Western blot and semi-quantitative analysis revealed dose-dependent upregulation of p21 and p16 in the 500 μM group versus controls (Figure 5B and C). These results were further validated by immunofluorescence staining, and semi-quantitative analysis revealed markedly elevated expression levels of senescence-associated proteins p21 and p16 in the 500 μM H_2O_2 group compared to the control, with enhanced green fluorescence intensity indicating robust protein accumulation (Figure 5D–G). Collectively, H_2O_2 treatment significantly promotes p21 and p16 expression in a concentration-dependent manner, accelerating AC senescence.

3.4. Construction and functional characterization of a 3D-bioprinted cartilage senescence model

The protocol for inducing AC senescence was optimized to 500 μM H_2O_2 for 2 h, as previously validated. After inducing senescence in the 3D-bioprinted cartilage model enriched with approximately 3 × 10^6 ACs, sterile PBS was used to rinse away residual H_2O_2. The 3D bioprinting technology enabled the construction of aging models that more accurately simulate the intracellular environment, increase cell interaction with biogenic ECM, and improve the stability and accuracy of senescence phenotype.[69] This study assessed p21 and p16 expression levels through Western blot and immunofluorescence staining, with semi-quantitative evaluation using ImageJ software. As displayed in Figure 6A, Western blot and semi-quantitative analysis revealed dose-dependent upregulation of p21 and p16 in the 500 μM group versus controls (Figure 6B and C). These results were further validated by immunofluorescence staining, and semi-quantitative analysis revealed markedly elevated expression levels of senescence-associated proteins p21 and p16 in the 500 μM H_2O_2 group compared to the control, with enhanced green fluorescence intensity indicating substantial protein accumulation (Figure 6D–G). These results suggest that H_2O_2 accelerates senescence in cartilage models through oxidative stress responses.

To further evaluate alterations in COL2 content within the 3D-bioprinted cartilage models of the control and 500 μM groups, semi-quantitative analysis was performed using immunofluorescence techniques. As illustrated in Figure 7A and B, immunofluorescence staining and semi-quantitative evaluation demonstrated a statistically significant reduction in COL2 expression in the 500 μM group compared to the control, indicative of oxidative stress-induced degradation of the cartilage matrix. Collectively, the semi-quantitative assessment of COL2 highlights the dual impact of oxidative stress on both cellular senescence and ECM disruption in the 3D-bioprinted cartilage model, thereby advancing our mechanistic understanding of pathological cartilage aging processes.

4. Conclusion

In this study, three different concentration ratios of Gel–Alg natural polymer hydrogels (7 Gel–3 Alg, 8 Gel–2 Alg, and 9 Gel–1 Alg) were used as tissue engineering scaffolds. Primary ACs served as seed cells and were combined with 3D bioprinting technology to construct cartilage models. Among the tested concentrations, the optimal hydrogel concentration ratio was identified as 7 Gel–3 Alg. Compared to the 8 Gel–2 Alg and 9 Gel–1 Alg hydrogel scaffolds, the 7 Gel–3 Alg hydrogel scaffold exhibited excellent biocompatibility, mechanical properties, and biological functions, such as promoting ECM secretion. Furthermore, 2D AC senescence models and 3D-bioprinted cartilage

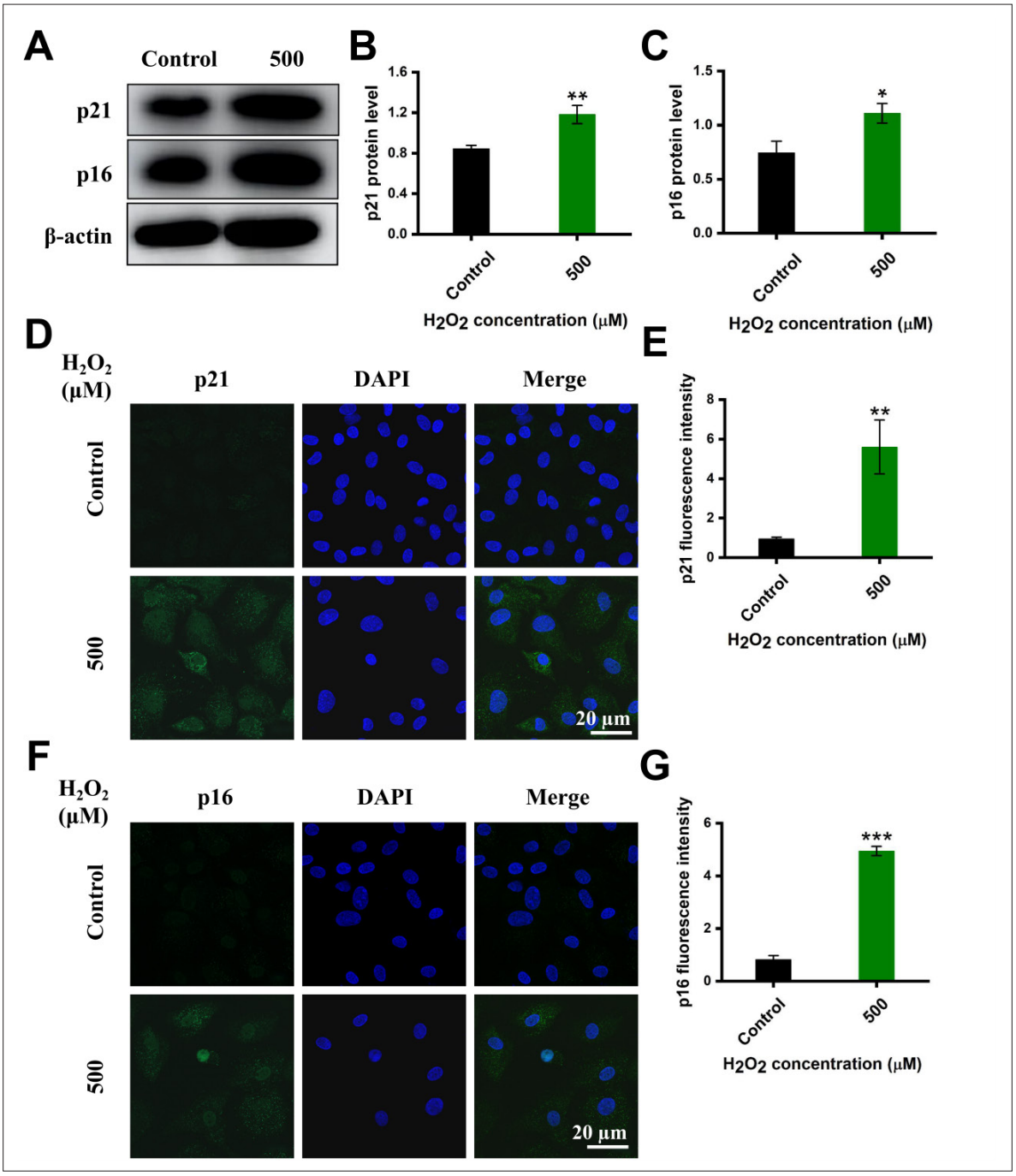

Figure 5. H_2O_2 promotes the expression of senescence-associated proteins p21 and p16 in a 2D AC senescence model. (A) Western blot analysis of p21 and p16 in the 2D AC senescence model. (B and C) Summary of quantitative data of p21 (B) and p16 (C) in the 2D AC senescence model. (D and E) Immunofluorescence staining analysis (D) and summary of quantitative data (E) of p21 in the 2D AC senescence model. (F and G) Immunofluorescence staining analysis (F) and summary of quantitative data (G) of p16 in the 2D AC senescence model. All statistical data are represented as mean ± standard deviation ($n = 3$; $^*p < 0.05$, $^{**}p < 0.01$, $^{***}p < 0.001$). Scale bars: 20 μm (D and F). Abbreviation: AC, articular chondrocyte.

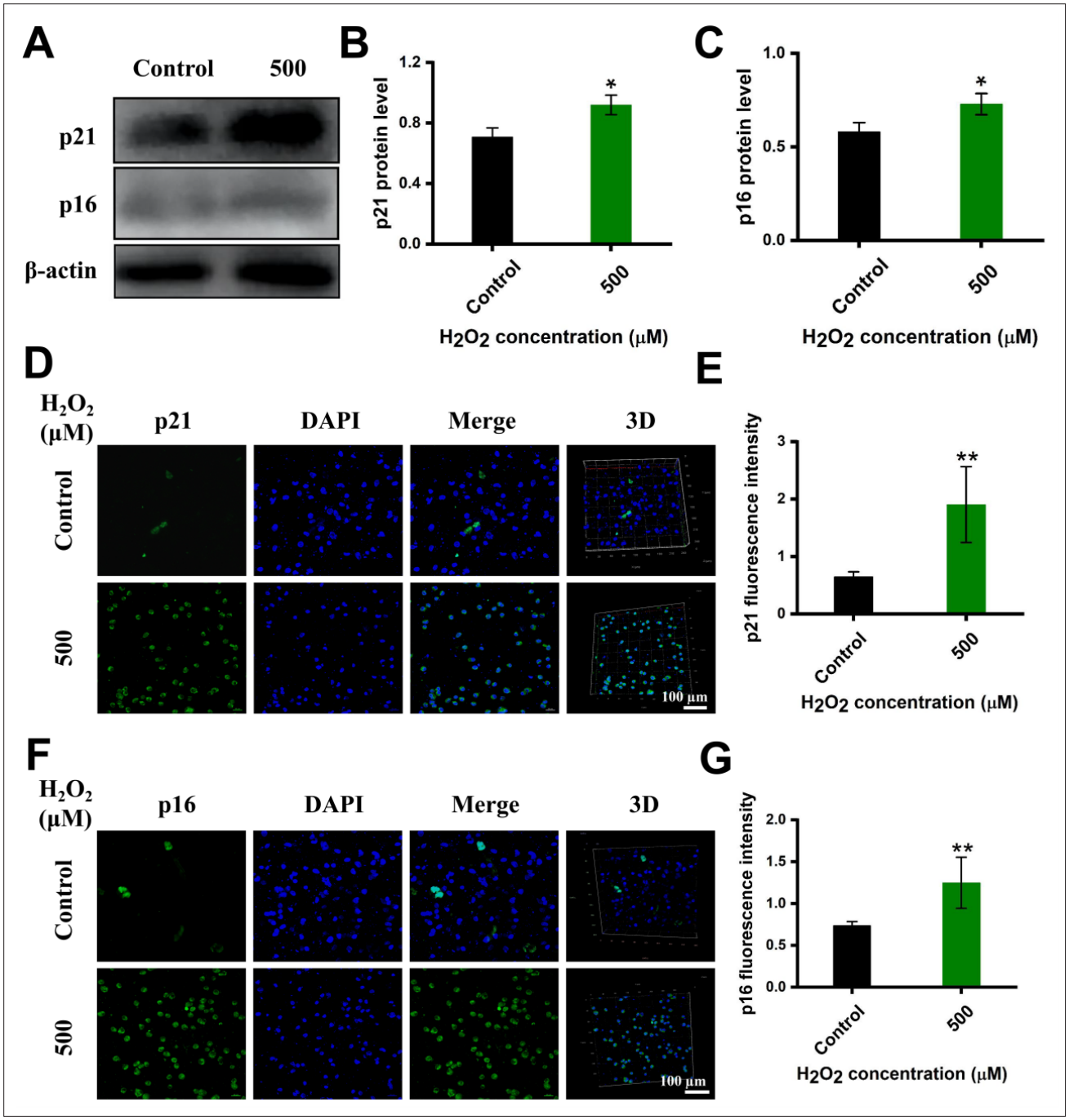

Figure 6. H_2O_2 promotes the expression of senescence-associated proteins p21 and p16 in a 3D-bioprinted cartilage senescence model. (A) Western blot analysis of p21 and p16 in the 3D-bioprinted cartilage senescence models. (B and C) Summary of quantitative data of p21 (B) and p16 (C) in the 3D-bioprinted cartilage senescence models. (D and E) Immunofluorescence staining analysis (D) and summary of quantitative data (E) of p21 in the 3D-bioprinted cartilage senescence models. (F and G) Immunofluorescence staining analysis (F) and summary of quantitative data (G) of p16 in the 3D-bioprinted cartilage senescence models. All statistical data are represented as mean ± standard deviation ($n = 3$; $^*p < 0.05$, $^{**}p < 0.01$). Scale bars: 100 μm (D and F).

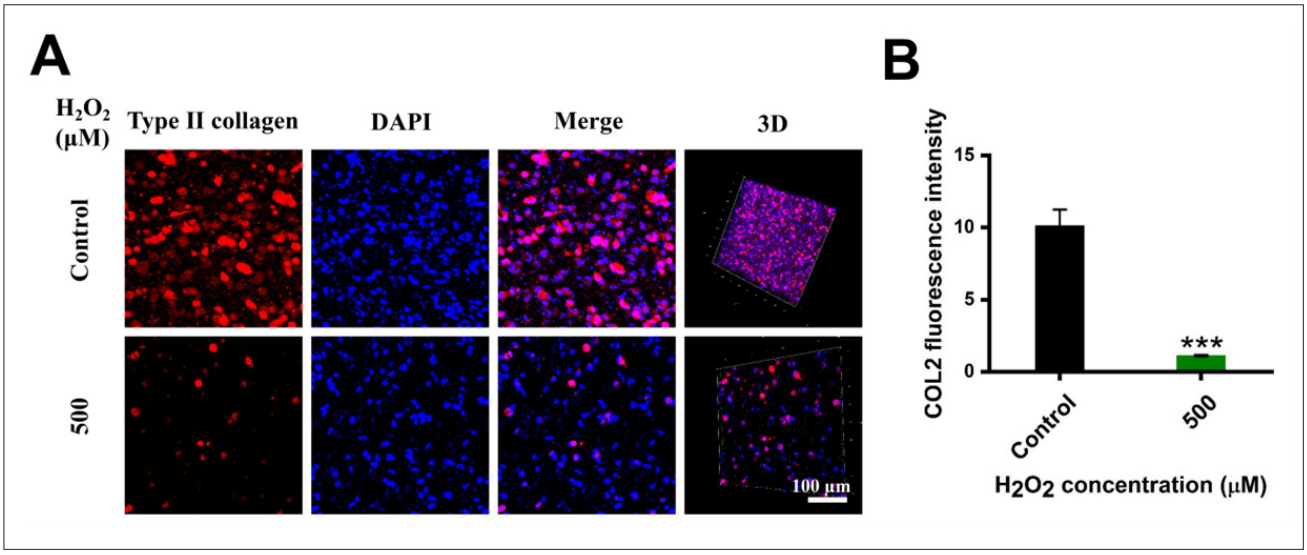

Figure 7. H_2O_2 reduces the expression of type II collagen in the 3D-bioprinted cartilage senescence model. Immunofluorescence staining analysis (A) and summary of quantitative data (B) for type II collagen in the 3D-bioprinted cartilage senescence models. All statistical data are represented as mean ± standard deviation ($n = 3$; ***$p < 0.001$). Scale bar: 100 μm.

senescence models were developed, and the optimal H_2O_2 concentration and induction time for constructing the senescence models were determined to be 500 μM and 2 h, respectively. Compared to the 2D AC senescence models, the 3D-bioprinted cartilage senescence models more closely resembled the natural aging state of human cartilage in terms of aging-related molecular expression. However, this study used SD rat ACs instead of humans and lacked comprehensive characterization of aging-related markers, including inflammatory factors and senescence-related proteins. These limitations reduce the translational relevance of the model for elucidating the mechanisms underlying OA development in humans. Future work should focus on developing more human-compatible *in vitro* OA models. Overall, the 3D-bioprinted cartilage senescence model may provide a valuable new experimental platform for research on the prevention and treatment of aging-related OA and the mechanisms underlying its development and progression.[70–72]

Acknowledgments

The authors are grateful to the Core Technology Platform of the Hangzhou Institute of Medicine Chinese Academy of Sciences for providing the essential resources for this study.

Funding

This study was supported by the Shenzhen Science and Technology Innovation Committee (JCYJ20230807110259002 and JCYJ20240813150201003) and the Ganzhou Municipal Science and Technology Project (2022-YB1396).

Conflict of interest

The authors declare no conflicts of interest.

Author contributions

Conceptualization: Hanxiao Qin
Formal analysis: Hanxiao Qin, Fanqing Xu
Investigation: Hanxiao Qin, Fanqing Xu
Methodology: All authors
Writing–original draft: Hanxiao Qin
Writing–review & editing: All authors
All the authors have read and approved the final manuscript.

Ethics approval and consent to participate

The animal experiments were conducted in accordance with the "Regulations on the Management of Experimental Animals" and were approved by the Experimental Animal Ethics Committee of Hangzhou Institute of Medicine Chinese Academy of Sciences (approval no. 2023R0025).

Consent for publication

Not applicable.

Availability of data

Data is available from the corresponding author upon reasonable request.

References

1. Li Y, Li L, Wang M, et al. O-alg-THAM/gel hydrogels functionalized with engineered microspheres based on mesenchymal stem cell secretion recruit endogenous stem cells for cartilage repair. *Bioact Mater*. 2023;28(5):255-272. doi: 10.1016/j.bioactmat.2023.05.003.
2. Guo X, Xi L, Yu M, et al. Regeneration of articular cartilage defects: therapeutic strategies and perspectives. *Tissue Eng Rev*. 2023;14(3):20417314231164765. doi: 10.1177/20417314231164765.
3. Liu Z, Lu T, Ma L, et al. DNA demethylation of promoter region orchestrates SPI-1-induced ADAMTS-5 expression in articular cartilage of osteoarthritis mice. *J Cell Physiol*. 2024;239(2):e31170. doi: 10.1002/jcp.31170.
4. Bank NC, Sanghvi P, Hecht CJ, et al. The epidemiology of posttraumatic osteoarthritis of the knee in the United States: an analysis of 948,853 patients from 2000 to 2022. *J Am Acad Orthop Surg*. 2024;32(7):313-320. doi: 10.5435/JAAOS-D-23-00662.
5. Zhang XX, He SH, Liang X, et al. Aging, cell senescence, the pathogenesis and targeted therapies of osteoarthritis. *Front Pharmacol*. 2021;12:728100. doi: 10.3389/fphar.2021.728100.
6. Loeser RF. Aging processes and the development of osteoarthritis. *Curr Opin Rheumatol*. 2013;25(1):108-113. doi: 10.1097/BOR.0b013e32835a9428.
7. June RK, Liu-Bryan R, Long F, et al. Emerging role of metabolic signaling in synovial joint remodeling and osteoarthritis. *J Orthop Res*. 2016;34(12):2048-2058. doi: 10.1002/jor.23420.
8. Ray A, Ray BK. An inflammation-responsive transcription factor in the pathophysiology of osteoarthritis. *Biorheology*. 2008;45(3-4):399-409.
9. Yang Y, Zhao X, Wang S, et al. Ultra-durable cell-free bioactive hydrogel with fast shape memory and on-demand drug release for cartilage regeneration. *Nat Commun*. 2023;14(1):7771. doi: 10.1038/s41467-023-43334-8.
10. Hu Y, Lyu C, Teng L, et al. Glycopolypeptide hydrogels with adjustable enzyme-triggered degradation: a novel proteoglycans analogue to repair articular-cartilage defects. *Mater Today Bio*. 2023;20(5):100659. doi: 10.1016/j.mtbio.2023.100659.
11. Zeng Q, Gong Y, Zhu N, et al. Lipids and lipid metabolism in cellular senescence: emerging targets for age-related diseases. *Ageing Res Rev*. 2024;97(6):102294. doi: 10.1016/j.arr.2024.102294.
12. Jimenez PA, Glasson SS, Trubetskoy OV, et al. Spontaneous osteoarthritis in Dunkin Hartley guinea pigs: histologic, radiologic, and biochemical changes. *Lab Anim Sci*. 1997;47(6):598-601.
13. Säämänen AK, Salminen HJ, Dean PB, et al. Osteoarthritis-like lesions in transgenic mice harboring a small deletion mutation in type II collagen gene. *Osteoarthritis Cartilage*. 2000;8(4):248-257. doi: 10.1053/joca.2000.0298.
14. Murakami T, Ishida T, Tanaka S, et al. Inflammation and subsequent nociceptor sensitization in the bone marrow are involved in an animal model of osteoarthritis pain. *Life Sci*. 2023;324(7):121736. doi: 10.1016/j.lfs.2023.121736.
15. Seo JE, Le Y, Revollo J, et al. Evaluating the mutagenicity of N-nitrosodimethylamine in 2D and 3D HepaRG cell cultures using error-corrected next generation sequencing. *Arch Toxicol*. 2024;98(6):1919-1935. doi: 10.1007/s00204-024-03731-4.
16. Yagi M, Endo K, Komori K, et al. Comparison of the effects of oxidative and inflammatory stresses on rat chondrocyte senescence. *Sci Rep*. 2023;13(1):7697. doi: 10.1038/s41598-023-34825-1.
17. Shboul SA, DeLuca VA, Dweiri YA, et al. Can 3D bioprinting solve the mystery of senescence in cancer therapy? *Ageing Res Rev*. 2022;81(11):101732. doi: 10.1016/j.arr.2022.101732.
18. Żuchowska A, Baranowska P, Flont M, et al. Review: 3D cell models for organ-on-a-chip applications. *Anal Chim Acta*. 2024;1301(5):342413. doi: 10.1016/j.aca.2024.342413.
19. Ziadlou R, Barbero A, Martin I, et al. Anti-inflammatory and chondroprotective effects of vanillic acid and epimedin C in human osteoarthritic chondrocytes. *Biomolecules*. 2020;10(6):932. doi: 10.3390/biom10060932.
20. Huang S, Song X, Li T, et al. Pellet coculture of osteoarthritic chondrocytes and infrapatellar fat pad-derived mesenchymal stem cells with chitosan/hyaluronic acid nanoparticles promotes chondrogenic differentiation. *Stem Cell Res Ther*. 2017;8(1):264. doi: 10.1186/s13287-017-0719-7.
21. Stüdle C, Vallmajó-Martín Q, Haumer A, et al. Spatially confined induction of endochondral ossification by functionalized hydrogels for ectopic engineering of osteochondral tissues. *Biomaterials*. 2018;171(7):219-229. doi: 10.1016/j.biomaterials.2018.04.025.
22. Castro-Viñuelas R, Viudes-Sarrión N, Rojo-García AV, et al. Mechanical loading rescues mechanoresponsiveness in a human osteoarthritis explant model despite Wnt activation. *Osteoarthritis Cartilage*. 2025;33(6):692-702. doi: 10.1016/j.joca.2024.02.945.
23. Byron CR, Trahan RA. Comparison of the effects of interleukin-1 on equine articular cartilage explants and

cocultures of osteochondral and synovial explants. *Front Vet Sci*. 2017;4(9):152.
doi: 10.3389/fvets.2017.00152.

24. Lin H, Lozito TP, Alexander PG, et al. Stem cell-based microphysiological osteochondral system to model tissue response to interleukin-1beta. *Mol Pharm*. 2014;11(7):2203-2212.
doi: 10.1021/mp500136b.

25. Dönges L, Damle A, Mainardi A, et al. Engineered human osteoarthritic cartilage organoids. *Biomaterials*. 2024;308(7):122549.
doi: 10.1016/j.biomaterials.2024.122549.

26. Hall GN, Mendes LF, Gklava C, et al. Developmentally engineered callus organoid bioassemblies exhibit predictive in vivo long bone healing. *Adv Sci (Weinh)*. 2020;7(2):1902295.
doi: 10.1002/advs.201902295.

27. SunY, You Y, Wu Q, et al. Genetically inspired organoids prevent joint degeneration and alleviate chondrocyte senescence via Col11a1-HIF1alpha-mediated glycolysis-OXPHOS metabolism shift. *Clin Transl Med*. 2024;14(2):e1574.
doi: 10.1002/ctm2.1574.

28. Shen C, Wang J, Li G, et al. Boosting cartilage repair with silk fibroin-DNA hydrogel-based cartilage organoid precursor. *Bioact Mater*. 2024;35(2):429-444.
doi: 10.1016/j.bioactmat.2024.02.016.

29. Thompson CL, Hopkins T, Bevan C, et al. Human vascularised synovium-on-a-chip: a mechanically stimulated, microfluidic model to investigate synovial inflammation and monocyte recruitment. *Biomed Mater*. 2023;18(6):065013.
doi: 10.1088/1748-605X/acf976.

30. Lin Z, Li Z, Li EN, et al. Osteochondral tissue chip derived from iPSCs: modeling OA pathologies and testing drugs. *Front Bioeng Biotechnol*. 2019;7(12):411.
doi: 10.3389/fbioe.2019.00411.

31. Ong LJY, Fan X, Sun AR, et al. Controlling microenvironments with organs-on-chips for osteoarthritis modelling. *Cells*. 2023;12(4):579.
doi: 10.3390/cells12040579.

32. Rothbauer M, Reihs EI, Fischer A, et al. A progress report and roadmap for microphysiological systems and organ-on-a-chip technologies to be more predictive models in human (knee) osteoarthritis. *Front Bioeng Biotechnol*. 2022;10(6):886360.
doi: 10.3389/fbioe.2022.886360.

33. Nu Aye KT, Ferreira JN, Chaweewannakorn C, et al. Advances in the application of iron oxide nanoparticles (IONs and SPIONs) in three-dimensional cell culture systems. *SLAS Technol*. 2024;29(3):100132.
doi: 10.1016/j.slast.2024.100132.

34. Wu KY, Tabari A, Mazerolle E, et al. Towards precision ophthalmology: the role of 3D printing and bioprinting in oculoplastic surgery, retinal, corneal, and glaucoma treatment. *Biomimetics (Basel)*. 2024;9(3):145.
doi: 10.3390/biomimetics9030145.

35. Jiu J, Liu H, Li D, et al. 3D bioprinting approaches for spinal cord injury repair. *Biofabrication*. 2024;16(3):032003.
doi: 10.1088/1758-5090.

36. Das S, Valoor R, Ratnayake P, et al. Bioprinting complex cartilaginous structures with clinically compliant biomaterials. *Adv Funct Mater*. 2015;25(48):7406-7417.
doi: 10.1021/acsabm.3c01194.

37. Schuurman W, Levett PA, Pot MW, et al. Gelatin–methacrylamide hydrogels as potential biomaterials for fabrication of tissue-engineered cartilage constructs. *Macromol Biosci*. 2013; 13(5):551-561.
doi: 10.1002/mabi.201200471.

38. Ávila HM, Schwarz S, Rotter N, et al. 3D bioprinting of human chondrocyte-laden nanocellulose hydrogels for patient-specific auricular cartilage regeneration. *Bioprinting*. 2016;1–2:22-35.
doi: 10.1016/j.bprint.2016.08.003.

39. Markstedt K, Mantas A, Tournier I, et al. 3D Bioprinting human chondrocytes with nanocellulose–alginate bioink for cartilage tissue engineering applications. *Biomacromolecules*. 2015;16(5):1489-1496.
doi: 10.1021/acs.biomac.5b00188.

40. Rastogi P, Kandasubramanian B Review of alginate-based hydrogel bioprinting for application in tissue engineering. *Biofabrication*. 2019;11(4):042001.
doi: 10.1088/1758-5090/ab331e.

41. Zhang X, Liu K, Qin M, et al. Abundant tannic acid modified gelatin/sodium alginate biocomposite hydrogels with high toughness, antifreezing, antioxidant and antibacterial properties. *Carbohydr Polym*. 2023;309(6):120702.
doi: 10.1016/j.carbpol.2023.120702.

42. Lai Y, Cao H, Wang X, et al. Porous composite scaffold incorporating osteogenic phytomolecule icariin for promoting skeletal regeneration in challenging osteonecrotic bone in rabbits. *Biomaterials*. 2018;153(1):1-13.
doi: 10.1016/j.biomaterials.2017.10.025.

43. Liu Z, Fang R, Meng Q The method of type II collagenase digestion can quickly obtain a large number of highly purified rat articular cartilage cells. *J Clin Rehabil Tissue Eng Res*. 2011;15(10):9323-9326.
doi: 10.3969/j.issn.1673-8225.2011.50.004.

44. Chen W, Xu Y, Li Y, et al. 3D printing electrospinning fiber-reinforced decellularized extracellular matrix for cartilage regeneration. *Chem Eng J*. 2020;15(2):122986.
doi: 10.1016/j.cej.2019.122986.

45. Wu Y, (William) Lin ZY, Wenger AC, et al. 3D bioprinting of liver-mimetic construct with alginate/cellulose nanocrystal hybrid bioink. *Bioprinting*. 2018;9(3):1-6. doi: 10.1016/j.bprint.2017.12.001.

46. Chung JHY, Naficy S, Yue Z, et al. Bio-ink properties and printability for extrusion printing living cells. *Biomater Sci*. 2013;1(7):763-773. doi: 10.1039/c3bm00012e.

47. Duan B, Hockaday LA, Kang KH, et al. 3D bioprinting of heterogeneous aortic valve conduits with alginate/gelatin hydrogels. *Biomed Mater Res*. 2013;101(5):1255-1264. doi: 10.1002/jbm.a.34420.

48. Ferris CJ, Gilmore KJ, Beirne S, et al. Bio-ink for on-demand printing of living cells. *Biomater Sci*. 2013;1(2):224-230. doi: 10.1039/c2bm00114d.

49. Skardal A, Atala A. Biomaterials for integration with 3-D bioprinting. *Ann Biomed Eng*. 2015;43(3):730-746. doi: 10.1007/s10439-014-1207-1.

50. Hu W, Wang Z, Xiao Y, et al. Advances in crosslinking strategies of biomedical hydrogels. *Biomater Sci*. 2019;7(3):843-855. doi: 10.1039/c8bm01246f.

51. Shanto PC, Al Fahad Md A, Jung HI, et al. Multi-functional dual-layer nanofibrous membrane for prevention of postoperative pancreatic leakage. *Biomaterials*. 2024;307(6):122508. doi: 10.1016/j.biomaterials.2024.122508.

52. Mohamadhoseini M, Mohamadnia Z. Alginate-based self-healing hydrogels assembled by dual cross-linking strategy: fabrication and evaluation of mechanical properties. *Int J Biol Macromol*. 2021;191(11):139-151. doi: 10.1016/j.ijbiomac.2021.09.062.

53. Miri AK, Khalilpour A, Cecen B, et al. Multiscale bioprinting of vascularized models. *Biomaterials*. 2019;198(4):204-216. doi: 10.1016/j.biomaterials.2018.08.006.

54. Bhaladhare S, Bhattacharjee S. Chemical, physical, and biological stimuli responsive nanogels for biomedical applications (mechanisms, concepts, and advancements): a review. *Int J Biol Macromol*. 2023;226(1):535-553. doi: 10.1016/j.ijbiomac.2022.12.076.

55. Giuseppe MD, Law N, Webb B, et al. Mechanical behaviour of alginate-gelatin hydrogels for 3D bioprinting. *J Mech Behav Biomed Mater*. 2018;79(3):150-157. doi: 10.1016/j.jmbbm.2017.12.018.

56. Caliari SR, Burdick JA. A practical guide to hydrogels for cell culture. *Nat Methods*. 2016;13(5):405-414. doi: 10.1038/nmeth.3839.

57. Mahmoudi C, Douma NT, Mahmoudi H, et al. Developing and characterizing a biocompatible hydrogel obtained by cross-linking gelatin with oxidized sodium alginate for potential biomedical applications. *Polymers (Basel)*. 2024;16(22):3143. doi: 10.3390/polym16223143.

58. Schwarz S, Kuth S, Distler T, et al. 3D printing and characterization of human nasoseptal chondrocytes laden dual crosslinked oxidized alginate-gelatin hydrogels for cartilage repair approaches. *Mater Sci Eng*. 2020;116(11):111189. doi: 10.1016/j.msec.2020.111189.

59. Zhao P, Deng C, Xu H, et al. Fabrication of photo-crosslinked chitosan gelatin scaffold in sodium alginate hydrogel for chondrocyte culture. *Bio Med Mater Eng*. 2014;24(1):633-641. doi: 10.3233/bme-130851.

60. Xu HQ, Liu JC, Zhang ZY, et al. A review on cell damage, viability, and functionality during 3D bioprinting. *Mil Med Res*. 2022;9(1):70. doi: 10.1186/s40779-022-00429-5.

61. Shi P, Laude A, Yeong WY. Investigation of cell viability and morphology in 3D bio-printed alginate constructs with tunable stiffness. *J Biomed Mater Res*. 2017;105(4):1009-1018. doi: 10.1002/jbm.a.35971.

62. Soltan N, Ning L, Mohabatpour F, et al. Printability and cell viability in bioprinting alginate dialdehydegelatin scaffolds. *ACS Biomater Sci Eng*. 2019;5(6):2976-2987. doi: 10.1021/acsbiomaterials.9b00167.

63. Coryell PR, Diekman BO, Loeser RF. Mechanisms and therapeutic implications of cellular senescence in osteoarthritis. *Nat Rev Rheumatol*. 2021;17(1):47-57. doi: 10.1038/s41584-020-00533-7.

64. Lou C, Deng A, Zheng H, et al. Pinitol suppresses TNF-α-induced chondrocyte senescence. *Cytokine*. 2020;130:155047. doi: 10.1016/j.cyto.2020.155047.

65. Arra M, Swarnkar G, Ke K, et al. Generation in chondrocytes is a potential therapeutic target for osteoarthritis. *Nat Commun.* 2020;11(1):3427. doi: 10.1038/s41467-020-17242-0.

66. Ma MW, Wang J, Zhang Q, et al. NADPH oxidase in brain injury and neurodegenerative disorders. *Mol Neurodegener.* 2017;12(1):7. doi: 10.1186/s13024-017-0150-7.

67. Liang H, Luo R, Li G, et al. The proteolysis of ECM in intervertebral disc degeneration. *Int J Mol Sci*. 2022;23(3):1715. doi: 10.3390/ijms23031715.

68. Coppé JP, Desprez PY, Krtolica A, et al. The senescence-associated secretory phenotype: the dark side of tumor suppression. *Annu Rev Pathol*. 2010;5:99-118. doi: 10.1146/annurev-pathol-121808-102144.

69. Sun Y, Wu Q, Dai K, et al. Generating 3D-cultured organoids for preclinical modeling and treatment of degenerative joint disease. *Signal Transduct Target Ther*. 2021;6(1):380. doi: 10.1038/s41392-021-00675-4.

70. Gao F, Xu Z, Liang Q, et al. Osteochondral regeneration with 3D-printed biodegradable high-strength supramolecular polymer reinforced-gelatin hydrogel scaffolds. *Adv Sci*. 2019;6(15):1900867.
doi: 10.1002/advs.201900867.

71. Gao F, Xu Z, Liang Q, et al. Direct 3D printing of high strength biohybrid gradient hydrogel scaffolds for efficient repair of osteochondral defect. *Adv Funct Mater*. 2018;28(13): 1706644.
doi: 10.1002/adfm.201706644.

72. Chen D, Wu JY, Kennedy KM, et al. Tissue engineered autologous cartilage-bone grafts for temporomandibular joint regeneration. *Sci Transl Med*. 2020;12(565):eabb6683.
doi: 10.1126/scitranslmed.abb6683.